Optical Engineering

OpticalEngineering.SPIEDigitalLibrary.org

Optimization of eyesafe avalanche photodiode lidar for automobile safety and autonomous navigation systems

George M. Williams, Jr.

SPIE.

George M. Williams, Jr. "Optimization of eyesafe avalanche photodiode lidar for automobile safety and autonomous navigation systems," *Opt. Eng.* **56**(3), 031224 (2017), doi: 10.1117/1.OE.56.3.031224.

Optimization of eyesafe avalanche photodiode lidar for automobile safety and autonomous navigation systems

George M. Williams Jr.*
Voxtel Inc., Beaverton, Oregon, United States

Abstract. Newly emerging accident-reducing, driver-assistance, and autonomous-navigation technology for automobiles is based on real-time three-dimensional mapping and object detection, tracking, and classification using lidar sensors. Yet, the lack of lidar sensors suitable for meeting application requirements appreciably limits practical widespread use of lidar in trucking, public livery, consumer cars, and fleet automobiles. To address this need, a system-engineering perspective to eyesafe lidar-system design for high-level advanced driver-assistance sensor systems and a design trade study including 1.5-μm spot-scanned, line-scanned, and flash-lidar systems are presented. A cost-effective lidar instrument design is then proposed based on high-repetition-rate diode-pumped solid-state lasers and high-gain, low-excess-noise InGaAs avalanche photodiode receivers and focal plane arrays. Using probabilistic receiver-operating-characteristic analysis, derived from measured component performance, a compact lidar system is proposed that is capable of 220 m ranging with 5-cm accuracy, which can be readily scaled to a 360-deg field of regard. [DOI: 10.1117/1.OE.56.3.031224]

Keywords: automobile driver-assistance sensor; avalanche photodiode; autonomous navigation; ladar; laser radar; lidar; laser imaging.

Paper 161243SS received Aug. 4, 2016; accepted for publication Feb. 1, 2017; published online Mar. 28, 2017.

1 Introduction

The critical component to a new class of cost-effective, high-performance automobile driver-assistance sensor (ADAS) and autonomous driving system is a sensor that can capture—without motion distortion—range and intensity data that are accurate, high resolution, and able to be used to create extremely detailed, high-definition, three-dimensional (3-D) maps of surroundings in real time, including those that may be geo referenced to real-world coordinates. The market previously addressed several of these objectives with radar, ultrasound, and vision sensors. However, radar, while offering a range of 200 m or better, is expensive and lacks angular resolution; ultrasound lacks the necessary range and resolution capabilities; and vision sensors lack the necessary long-distance range performance. Compared with these current market solutions, eyesafe lidar sensors offer improved performance for long-distance object detection and mapping in low-visibility conditions, and allow compact, cost-effective sensor systems to be realized.

The benefits of lidar stem from the principles of its operation (e.g., Fig. 1). A lidar device shoots out rapid bursts of short pulsed infrared laser light, in a very similar fashion to sonar with sound waves or radar with radio waves. Unlike radar, which uses large radio-frequency waves and captures low-resolution 3-D images at no better than 0.5-m resolution, lidar uses optical waves, which have a length ~500× shorter and can capture higher resolution 3-D images with finer depth precision. The light travels toward whatever object is in its path, then reflects back toward the device. Since the speed of light is well known, lidar sensors can determine the range to a target by measuring the time it takes for the light to return to the origin. In this way, azimuth-elevation-range and range rate measurements may be captured. The use of reflected laser light also allows the reflectivity of objects to be measured—independent from ambient light—enabling lidar to provide long-distance high-fidelity range imaging in a wide range of conditions. Because lidar uses its own light source, it avoids the problems of video cameras, which do not operate well in dark conditions and are prone to high false-alarm rates (FARs) and saturation under brightly lit conditions.

While it is inevitable that the near future will bring autonomous-navigation and ADAS systems that play important roles in automobile safety and navigation, despite its significant promises, the role that lidar sensors will play, among the suite of sensors, is yet to be determined. Existing automobile lidar sensors have yet to achieve the necessary range and resolution performance in inclement conditions, and significant improvements need to be made on lidar system size, weight, and power, as well as cost and reliability. The lack of suitable lidar instruments appreciably limits practical widespread use of lidar in a wider range of ADAS applications, and arguably has slowed the proliferation of level 3, and higher, automated driving systems.[1]

The holy grail of a lidar sensor is a reliable low-cost all-weather camera that is capable of capturing temporally registered and calibrated, high dimensionality angle-angle-range point cloud data fully from around the vehicle (360 deg) using nonmechanical scanning—with a sufficiently fast update rate to avoid vehicle motion artifacts and provide sub-ms response time. Rather than capturing just a single range return, the ideal lidar sensor might be configured to capture the reflectivity, pulse shape, polarization, and other scene attributes encoded in a return pulse waveform,

*Address all correspondence to: George M. Williams, E-mail: georgew@voxtel-inc.com

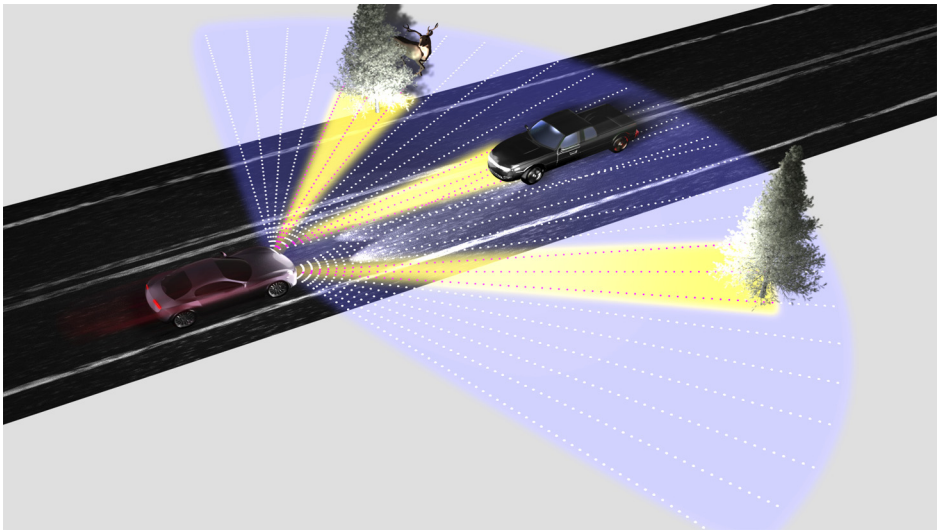

Fig. 1 Lidar bounces light beams off objects rather than using radio waves, as with radar. In an autonomous car, it works with radar and cameras to give the vehicle 360-deg vision of its surroundings.

to increase the dynamic information available to the system efficiently as a function of the average laser power expended.

Lidar applications can be grouped into two primary distance zones of interest: "a medium distance" of ~20 to 40 m for side and angular warning zones, and a "long distance" of 150 to 400 m for the front and rear. Medium distance lidars generally require multilocation placement and, as they need to fit within the body panels of the vehicle, size is an issue. To reduce the number of sensors needed, each must have a large field of view (FOV)—generally more than 100 deg in azimuth.

A long distance lidar has a field of regard (FOR) covering all, or a significant part, of the 360-deg azimuth, with an FOR in elevation that extends from the foot of a pedestrian located 1 m away to vehicles 400 m or farther down the road, resolved to better than 0.1-deg angular resolution and centimeter-scale range accuracy.

A notional long distance lidar sensor requirement is specified in Table 1. The challenge is to determine the lidar system architecture that best meets these requirements, given the available transmitter, receiver, and optical technologies.

While there are medium distance lidar systems on the market, there are currently no reliable long distance lidar systems. Currently available lidar systems can now scan up to only 120 m ahead—a level of performance inferior to the 500-m range capabilities of camera-based systems.[2] The Velodyne HD lidar system, for example, is a scanned lidar system. It uses 64 class-1, 905-nm laser diodes.[3] Depending on the resolution required, it rotates in the range of 300 to 900 RPM, allowing it to scan the 30 m of road in front of the vehicle (10% reflectivity) and sense the surrounding vehicles, pedestrians, and trees (80% reflectivity) to a distance of 120 m.[4] The 16-beam "Puck" version, model VLP-16, is 103 $mm^2 \times 72$ mm^2 in size, weighs 830 g, and provides 3-D data over a 360-deg scan in a 30-deg vertical angle with 100-m range capability, 8-W power consumption, and ±3-cm accuracy. It sells for ~$7999.[5]

In addition to the early market entrant Velodyne, a large number of vendors are entering the market, promising solid-state lidar below $1000.[4] For example, flash lidars integrating silicon-based photodetectors and capable of imaging in a 30-deg × 30-deg swath at ranges up to 30 m are promised at a cost below $100.[1] Also emerging in the market are multimodal sensors capable of both video imaging and 3-D lidar imaging.[6,7]

2 Selecting Operating Wavelength

The cost and performance of the current lidar systems can be traced to the choice of sensor architecture, based on the chosen laser transmitter and detector technologies. While use of commercially available 905-nm diodes is often attributed to its compatibility with cost-effective silicon detector technology, the large depletion depth of near-infrared optical radiation in silicon makes photodetectors manufactured using deep-submicron CMOS processes largely inefficient or slow to respond to pulsed 905-nm light. When a single detector element or a small detector array is used, detectors made of compound semiconductor materials, such as InGaAs, may pose minimal incremental contribution to cost, while offering enhanced temporal response and the possibility of using lasers that pose less ocular hazard.

Both the IEC-60825-1 and ANSI Z136.1 standards include methods to calculate maximum permissible exposure (MPE), and these methods depend on the operation of the transmitter and its implementation, which are governed by the most stringent safety-level requirement. The MPE levels for visible and near-infrared wavelengths are quite low. Collimated laser beams of 905-nm light are especially dangerous at relatively low powers because the lens focuses the light onto a tiny spot on the retina. At 905 nm, for a 1-ns pulse, the MPE at the cornea for a collimated laser beam of laser light is ~1$\mu J/cm^2$ of energy density, and ~5 mW/cm^2 power density for a 1-s exposure time.[8] Reducing ocular hazard necessitates either: limiting transmitter pulse energy, thereby degrading range performance and reducing performance in inclement weather; or expanding the transmitter optic, thereby increasing system size and weight.

To ensure the laser is fully eyesafe (class 1M, IEC/EN 60825), the maximum pulse energy and pulse-repetition rate must be limited, and an appropriate beam expander must be used.[9,10] At high repetition rates (i.e., above 55 kHz), the emission is considered as a continuous-wave source with

Table 1 Notional lidar sensor specifications for autonomous navigation.

Requirements	Specification	Units
Eye safety	Class 1	ANSI standards
Azimuth field of regard	360 (6.25)	deg (rad)
Elevation field of regard	20 (0.35)	deg (rad)
Angular resolution	0.02 (0.35)	deg (mrad)
Azimuth samples	18,000	elements
Elevation resolution elements	1000	elements
Frame format	1.8×10^7	elements/frame
Frame rate (scan rate)	20 (7200)	frames/s (deg/s)
FOR sample rate	3.6×10^8	samples/s
Maximum range	220	m
Minimum TOF to range	1.47×10^{-6}	s
Unambiguous laser pulse rate	6.82×10^5	Hz
Sample rate to laser rate ratio	528	sample elements/pulse
Range resolution/time precision	0.05/333	m/ps
Range-resolved elements	4400	time slices (~12 bits)
Returns per pulse	1(3)	minimum (desired)
Analog pulse digitization	8	bits
Min unencoded data bit rate—1 sample TOF and amp.	7.2×10^9	bits/s
Aperture	35	mm
Laser pulse energy required for 220-m sensitivity	0.2	micro-Joules (10% reflective target)
Laser pulse energy required for unambiguous data	105.6	micro-Joules
Average power required	72	W

a power level equal to the average power emitted by the transmitter. The safety requirements on these laser transmitters make it difficult to cover a large FOR, and expanding the laser beam to reduce the power flux density increases system size and weight.

In contrast, short-wavelength infrared (SWIR) light—with a wavelength longer than ~1400 nm—is absorbed by the transparent parts of the eye before it reaches the retina, which means that the MPE for these wavelengths is higher than for visible light. At ~1.5 μm, the MPE is ~1 J/cm^2, allowing for configuration with smaller-diameter collimator optics with higher radiant-intensity output than their 905-nm counterparts. This makes the 1.5-μm spectral range well-suited for scanned-linear, stepped two-dimensional (2-D) arrays, and full-format flash lidar systems. Eye safety is maintained for the high-brightness laser beams by low-duty-cycle pulsing and by the motion of the beam as it scans the FOV, such that the limits of optical power safety are not exceeded.

A further benefit of operating in the SWIR is that it provides less scattering from rain, smoke, smog, and other atmospheric elements, and is less susceptible to clutter due to inband solar radiation compared to 905-nm laser light.

These benefits can make use of higher pulse energy in small-area, scanning, or large-format detector arrays.

3 Eyesafe Lidar System Architectures

There are two general classes of lidar sensors—"scanning" and "flash." Most of today's lidar sensors are configured as single-element [i.e., one-dimensional (distance)] measurement devices combined with a mechanical beam-deflection system (e.g., a rotating mirror or scanning mirrors) to provide spatial measurements. Scanning-lidar and flash-lidar systems use the same technique to determine range to a target—that is, they measure the time of flight (TOF) of a laser pulse to the target and back to the detector. However, the illumination and detection approaches differ. "Scanning lidar" systems operate either by raster-scanning the laser spot over a region of the target surface, or by using the relative motion of the lidar platform with respect to the object. This process continues until the (x, y, z) coordinate and intensity of the entire FOR are measured. While scanning-lidar systems are very effective for scenes that are relatively static over time, they do not perform as well in dynamic situations in which rapid ranging and imaging of an entire scene are required.

An important operational parameter is the "ambiguity range," which is the range to an object, where the backscattered light from a given laser pulse is detected before the emission of the next laser pulse.[11,12] The ambiguity determines the maximum laser repetition rate—and, ultimately, the peak laser power and average laser power—and is, thus, an important system-design parameter. As shown in Table 1, the unambiguous laser-repetition rate, for 220-m range returns is 682 kHz—a rate that is 528× less than the ~360-MHz rate required to sample the 360-deg × 20-deg FOR with the specified resolution and update rate. The limitations imposed by the speed of light necessitate that either the system be segmented into 528 individual spot scanning lidar cameras, each with a small FOR, or that the laser output beam be matched to the solid angles subtended by ~528 photodetector elements. Obviously, when the divergence of the laser is increased, more peak power is required to maintain the specified standoff range and range resolution.

With sufficient laser pulse energy, mechanical movements to produce a timed illumination of an FOV can be eliminated by taking advantage of rapidly maturing focal-plane-array (FPA) technology to realize "flash-lidar" systems. With a flash-lidar system, the laser beam is diverged so that the illuminated spot on the surface closely matches the FOV of a 2-D array of detectors. In most realizations of flash lidar, the beam divergence of the laser is optically matched to the receiver FOV so that all pixels in the array are illuminated at

once. Each pixel in the detector array is individually triggered by the arrival of a pulse return generated within its instantaneous FOV, allowing for measurement of both intensity and TOF of one or more returns from the laser pulse. In this way, each pixel (x, y) has its own range data $(z_0, z_1, \ldots, z_{\text{last}})$ resulting in the 3-D point cloud. The resolution in x and y depends on the camera resolution, and the range resolution in z depends on the pulse width or rise time of the laser, the response time of the photodetector elements, and the resolution of the time-conversion circuits.

A clear advantage of a flash system over a scanning system is that it is faster to provide a full-scene frame. The frame rate is limited only by how fast the laser can be pulsed and how fast the pixel readout can occur. Moreover, the lower capacitance of the small pixels used in 2-D detector arrays allows for higher pixel-conversion gain and lower pixel-amplifier noise, which can improve sensitivity and range resolution. In this respect, a flash lidar FPA may have superior sensitivity in terms of average laser power, although the peak power required to illuminate a 2-D FPA scales proportionally to the pixel count.

Within the available trade space for practical lidar sensor designs are hybrids of the scanned and flash-lidar concepts that use either a small-sized linear or 2-D detector array with an FOV matched to the laser angular divergence, in which: the laser output and detector array are synchronously scanned across the FOR; or large-format 2-D detector arrays are used that are configured with bright, low-divergence, or beam-shaped fan lasers that scan across the detector array to create the lidar image.

4 Lidar Sensor Model

The notional lidar sensor specification in Table 1 describes a 360-deg (azimuth) by 20-deg (elevation) sensor, with 0.02-deg angular resolution (~7-cm footprint at 220 m), and 5-cm range resolution.

4.1 *Sensitivity*

The laser-beam shape, the transmit-pulse energy, and the propagation path of the light factor into what is received; atmospheric absorption and scattering attenuate the laser beam as it propagates, and turbulence can cause broadening, defocusing, and deflection. The target orientation, surface texture, and reflectivity properties also affect performance; for example, the geometric complexity of the surface and the Lambertian and specular components of the target's reflectivity determine how much energy is reflected back to the receiver's aperture, and the orientation of the target relative to the angle of incidence can lengthen the pulse and modulate its shape. Finally, the optical efficiency, the detector optical-to-electrical conversion efficiency, and the photoreceiver gain-bandwidth and sensitivity properties significantly influence system performance.

The amount of laser energy returned from multifaceted targets can be estimated as[13]

$$P_R = \frac{4KP_sT_A\eta_t}{\pi\phi^2R^2}\Gamma\frac{T_A}{4\pi R^2}\frac{\pi D^2\eta_r}{4}, \tag{1}$$

where P_R is the received signal power in watts; K is the beam profile function; P_S is the transmitted laser power in watts; T_A is atmospheric transmission; η_t is transmitter optical efficiency; Φ is beam width in radians, R is range (monostatic system); Γ is target laser cross section in meters; D is receiver aperture diameter; and η_r is receiver optical efficiency.

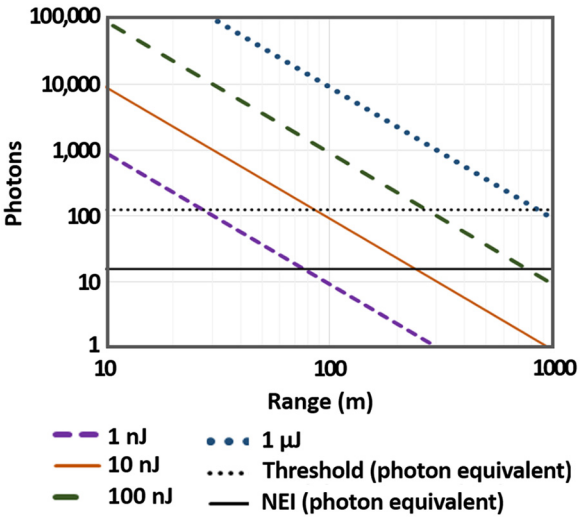

Fig. 2 Modeled photon returns for the lidar receiver for 1, 10, and 100 nJ, and 1-μJ pulse energies, assuming a 30-mm aperture, a 30% reflective target, and a 0.5-mrad divergent laser.

Equation (1) is useful for establishing a photon budget for use in performing system-design trade studies; the received signal power can easily be converted to photons for a given laser pulse duration, knowing the energy per photon. Figure 2 shows the photons expected from 30% reflective targets at various ranges, calculated for several laser pulse energies. Here, a 0.5-mrad laser divergence and a 30-mm diameter receiver with 70% optical efficiency are assumed.

One of the first parameters to choose when designing a lidar sensor is its threshold value (for instance, in voltage: V_{th}) given the noise level of the photoreceiver ($\sigma_{v,n}$), which must be computed from the specification on the probability of false alarm (PFA), i.e., the probability that a signal will be larger than the threshold in the absence of the target. The PFA and the FAR are related to each other by the fact that the number of false alarms over some time duration is the product of the false alarm rate per individual sample (PFA) by the number of samples being made during that time, as follows:

$$\text{PFA} = \text{FAR}(\text{for a given time})/\text{number of measurements during that time.} \tag{2}$$

As shown in Table 1, a 1.5-μs time-of-flight is required for 220-m range. For this scenario, a 60-Hz FAR implies that one in every 11,363 range samples will be corrupted by a false positive. For the lidar sensor specified in Table 1, this is roughly once per frame. Similarly, for a flash lidar configuration, if there are total pixels of N_{pixels} in an array, each characterized by the same FAR (in Hz), then Poisson statistics can be applied to find

$$P_{\text{FA}} = 1 - \exp(-\text{FAR} \times N_{\text{pixels}} \times t). \tag{3}$$

Using Eq. (3), the probability of at least one false alarm is equal to one minus the probability of zero false alarms; the argument of the exponential function is just the expected

number of false alarms from the entire array over the period of observation.

Rice[14,15] relates the single-pixel FAR to the bandwidth (BW, in Hz) of the analog signal into the comparator, the detection threshold (n_{th}, in electrons), and the magnitude of the noise on the signal into the comparator (n_{noise}, in electrons), as follows:

$$\text{FAR} = \sqrt{\frac{1}{3}}\text{BW}\,\exp\left[-\frac{n_{\text{th}}^2}{2n_{\text{noise}}^2}\right]. \tag{4}$$

Note that, physically speaking, both the detection threshold and the noisy signal into the pixel comparator are voltage quantities; for convenience of comparing signal levels, both quantities have been referred to the input node of the amplifier chain and expressed in units of electrons.

To find the condition restricting n_{th}, Eqs. (3) and (4) can be combined as follows:

$$n_{\text{th}} = \sqrt{-2n_{\text{noise}}^2\,\ln\left[-\frac{\sqrt{3}\,\ln(1-P_{\text{FA}})}{N_{\text{pixels}}\times\text{BW}\times t}\right]}. \tag{5}$$

The approximations generally hold true for photodiodes and large photon numbers, in which both the detector and amplification noise processed can be approximated as normal distributions. In these cases, the PFA is a rapidly decreasing function of the ratio, $v_{\text{th}}/\sigma_{v,n}$, between the threshold value and the standard deviation of the photoreceiver's dark noise.

However, the treatment of Eq. (5) is not adequate for avalanche photodiodes (APDs). All APDs generate excess noise due to the statistical nature of the avalanche process. The excess-noise factor (F) is the ratio of the mean square gain to the square of the mean gain; it is also the ratio by which the spectral intensity of shot noise on an APD's current exceeds that would be expected from a noiseless multiplier on the basis of Poisson statistics alone.

The excess-noise factor is a function of both the gain (M) and the APD's effective ionization coefficient ratio (k). The first-order statistics of the excess-noise factor are normally calculated using a formula derived by Mclntyre[16] which is based on the assumption of an avalanche medium with uniform characteristics and an impact-ionization process that is independent of carrier history, expressed as

$$F(M,K) = M\left[1-(1-k)\left(\frac{M-1}{M}\right)^2\right], \tag{6}$$

The excess shot noise of an APD at a given gain depends on its effective ionization coefficient ratio, according to Eq. (6). The values of the effective ionization coefficient ratio are significant because they correspond to different APD device technologies that are compatible with near-infrared-sensitive InGaAs absorbers. The most common InGaAs APDs have bulk InP multipliers characterized by $k = 0.4$. InGaAs APDs with thin InAlAs multipliers are characterized by $k<0.2$, and Voxtel, Inc., has developed InGaAs APDs with multiple gain stages that can operate with $k\tilde{}0.02$[17]

Most InGaAs APDs generate the majority of their primary dark current in their absorber, alongside the primary photocurrent generated by the optical signal and the background signals. In that case, dark carriers from primary dark current can be grouped with the background, as follows:

$$n_{Q,\text{dark}}^2 = n_{\text{amp}}^2 + \left(\left\langle a_{\text{dark}}\right\rangle + \left\langle a_{\text{background}}\right\rangle\right)M^2F(M), \tag{7}$$

where n_{amp}^2 is the noise from the amplifier, $\left\langle a_{\text{dark}}\right\rangle$ is the mean of the primary dark-current charge deposited during the effective integration time, and $\left\langle a_{\text{background}}\right\rangle$ is the primary background signal level within the effective integration time.

It is often overlooked that, for APD photoreceivers, normal statistical methods cannot be used to calculate PFA. The dark current signals from an APD photoreceiver resemble the pulse-height distribution of the multiplication process to the carriers; after avalanche multiplication, each primary carrier injected into an APD's multiplier may yield a different number of secondary carriers. For most linear-mode APDs, the statistical distribution of n output carriers resulting from an input of a primary carriers is that derived by McIntyre[18]

$$P_{\text{McIntyre}}(n) = \frac{a\Gamma\left[\frac{n}{1-k}+1\right]}{n(n-a)!\times\Gamma\left[\frac{nk}{1-k}+1+a\right]} \times\left[\frac{1+k(M-1)}{M}\right]^{a+\frac{nk}{1-k}}\times\left[\frac{(1-k)(M-1)}{M}\right]^{n-a}, \tag{8}$$

where k is the ratio of hole-to-electron impact-ionization rates, M is the average gain, and Γ is the Euler gamma function.

The McIntyre distribution has a pronounced positive skew. The importance of the value of k on the shape of the distribution and the resulting lidar receiver sensitivity is shown in Fig. 3. Figure 3 shows the dark count rates measured on an APD photoreceiver for the cases of APDs with $k = 0.2$ and $k = 0.02$, as a function of the threshold level. As shown in Fig. 3, top, at a gain of about 6, the high-gain events from the distribution of the $k = 0.2$ APD will start to dominate the FAR, limiting the threshold values for this particular receiver to greater than 0.53V for operation at 30-Hz FAR. However, in the case of the $k = 0.02$ APD (Fig. 3, bottom), even at gains of $M = 11$, the APD photoreceiver distribution is closer to Gaussian, and—for this particular receiver—the 30-Hz FAR can be achieved closer to 0.49 V.

At this voltage threshold level, the photon equivalent threshold level (n_{th}) can be calculated using the measured conversion gain of the receiver. The curves of Fig. 3 can be modeled for each APD bias by convolving the gain distribution with the amplifier noise to find the value of n_{th} for the target FAR.

Using a pulse time (τ), the product of noise current and integration time, scaled by the elementary charge, can be recognized as the total charge noise ($n_{Q,\text{dark}}$). These operations can be applied to find the FAR, as follows:

$$FAR_{McIntyre} = \sqrt{\frac{2\pi}{3}}BW * n_{Q,\text{dark}} * P_{RX}(n_{th})\quad [Hz]. \tag{9}$$

To find the probability of laser-pulse detection, P_{DE}, the detection threshold to achieve a given FAR can be combined with the average signal strength, based on the

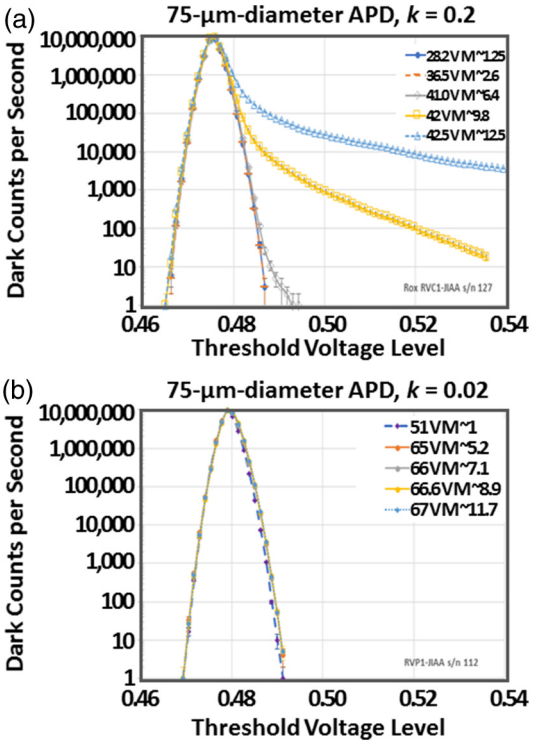

Fig. 3 Dark-output distribution of photoreceivers for the cases of (a) a $k = 0.2$ APD and (b) a $k = 0.02$ APD, showing the tails of the distribution due to the McIntyre-distribution function cause a significant increase in false counts, even at modest gain—much more than the Gaussian assumption.

complementary cumulative distribution function of the convolution of the signal and noise distributions, as

$$P_{\mathrm{DE}} = 0.5 - 0.5\,\mathrm{erf}\left[\frac{n_{\mathrm{th}} - \langle a_{\mathrm{signal}}\rangle/(M)}{\sqrt{2(n_{Q,\mathrm{dark}}^2 + \langle a_{\mathrm{signal}}\rangle/M^2F)}}\right], \quad (10)$$

where $\langle a_{\mathrm{signal}}\rangle$ is the mean effective equivalent primary signal in the junction, before avalanche multiplication. The equivalent photon signal level can be determined by converting $\langle a_{\mathrm{signal}}\rangle$ to the input of the APD absorber by dividing by the quantum efficiency.

4.2 *Time Resolution*

To capture the TOF, the detector elements must include circuitry to timestamps of the laser-pulse echoes. Achieving 5-cm range resolution requires timestamps with ~333-ps resolution. Timestamps can be generated using either: a time-to-analog converter, which records the timestamp by sampling a time-variable voltage ramp; or a time-to-digital converter, which—upon the return of the pulse—latches the digital value of a counter, often with a vernier scale, developed from gate-delay elements, used for the least significant bits. Jitter, walk, and drift are the three major factors limiting time resolution.

In the absence of noise and amplitude variations, the leading-edge discriminator would mark the arrival time of each analog pulse with precision and consistency. However, practical systems include a non-negligible level of electronic noise, and this noise causes an uncertainty—or "jitter"—when the analog pulse crosses the discriminator threshold. If σ_n is the voltage amplitude of the noise superimposed on the analog pulse, and dV/dt is the slope of the signal when its leading edge crosses the discriminator threshold, the contribution of the noise to the timing jitter is

$$\sigma_j = \sigma_n/(\mathrm{d}V/\mathrm{d}t). \quad (11)$$

As shown in Fig. 4, from Eq. (11), the relationship is immediately apparent between the signal amplitude, detector gain, and amplifier transimpedance gain on the timing accuracy. If the noise cannot be reduced, the minimum timing jitter is obtained by setting the discriminator threshold for the point of maximum slope on the analog pulse. Thus, preserving the fastest possible rise time from the signal source is a clear benefit.

"Time walk" is the systematic dependence of the timing on the amplitude of the input pulse. As shown in Fig. 4, with a leading-edge timing discriminator, smaller pulses produce

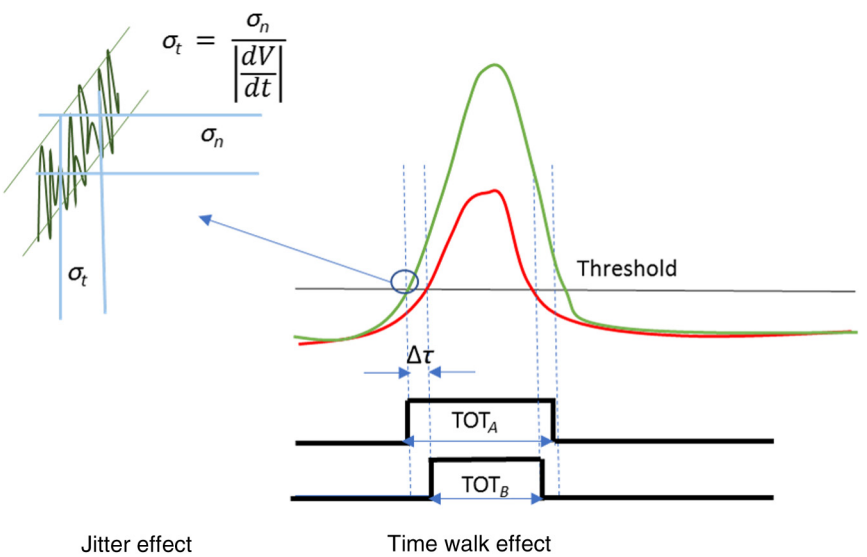

Fig. 4 Illustration of the time walk effect, including a time-over-threshold discriminator signal and a jitter effect.

an output from the discriminator later than larger pulses, leading to variable timing in response to the variations in the input pulse amplitudes. Obviously, when a wide range of pulse amplitudes must be processed, time walk can seriously degrade the time resolution. To ensure precise timing, time walk must be minimized or eliminated. The recommended techniques to minimize time walk include amplitude-compensated measurements implemented using pulse amplitude or time-over-threshold compensation, or by implementing a constant-fraction-discrimination circuit.

5 Lidar System Design

5.1 *Infrared Transmitter*

The available SWIR transmitter sources include edge-emitting pulsed semiconductor laser diodes, erbium-doped fiber lasers, and erbium-doped glass diode-pumped solid-state (DPSS) lasers, with the latter two choices best suited for long-range lidar. Fiber lasers allow the combination of short pulse durations with repetition rates up to ~1 million shots/s, at a practical upper pulse energy of ~1 μJ, whereas erbium-doped glass lasers can be configured for higher peak power, albeit generally with low repetition frequencies.

Figure 5 shows a prototype of a new compact, low-cost 1535-nm DPSS laser from Voxtel. We custom-developed this cost-effective 20-μJ pulse energy, 400-kHz pulse-rate laser for autonomous navigation lidar. This allows for an array to be stepped or scanned across the FOR. For example, when the 20-μJ pulses are matched to 200 detector elements, roughly 100 nJ per pulse, such that 220-m range can be achieved (see Fig. 2), ~80 million angle-angle-range vectors per second can be obtained—~1/9 which is required to meet the full FOR specified in Table 1.

5.2 *Lidar Photoreceivers*

As the photoreceiver sets the system sensitivity, its performance can obviously have dramatic effects on the required average laser power. Lidar photoreceivers typically comprise a photodetector, transimpedance amplifier (TIA), and pulse-detection circuit. At the 905-nm wavelength, the two primary solid-state photodetector options are silicon PIN photodiodes and silicon avalanche detectors. While, when compared to silicon, both InGaAs and germanium (Ge) detectors offer the potential for improved temporal response to 905-nm optical radiation, both detector types are more commonly operated at wavelengths beyond 1 μm, where silicon does not respond. For 1.5-μm operation, InGaAs photodiodes have higher bandwidth and less noise than Ge detectors.

Fig. 5 Picture of Voxtel's miniature 1535-nm DPSS laser, which has a beam quality of $M^2 < 1.1 * \mathrm{DL}$ (diffraction limit) and operates at 20 μJ at up to 400-kHz repetition rates.

To reduce the laser pulse energy requirements, APDs may be used. An APD is a special type of photodiode that amplifies photocurrent via an electron avalanche process. APDs can be operated in either linear mode or Geiger mode (GM). In GM operation, the APD is momentarily biased beyond its breakdown voltage, such that it may enter avalanche breakdown in response to signals as weak as a single photon. The penalty for the extreme sensitivity of GM is that GM APDs cannot measure the amplitude of multiphoton pulse returns, and they must be reset after firing before rearming. The dead time of a GM APD can span a few nanoseconds for silicon GM APDs to a few microseconds for InGaAs GM APDs. In 3-D-imaging applications, the dead time prevents single-laser-shot reception of multiple target returns from objects closely spaced in range and makes GM APDs susceptible to blinding by atmospheric backscattering or optical solar clutter. This hindrance limits the practical utility of GM APDs for practical commercial lidar applications, especially for InGaAs GM APDs.[19,20]

In linear-mode operation, the average output of the APD is proportional to the strength of the optical signal, and the detector can operate continuously. Common SWIR-sensitive linear-mode APDs operate with average avalanche gain of $\sim M < 50$, more typically at $M = 10$ to 20. Dark current is greater for the larger-diameter photodetectors typically used in scanned lidar systems, and the excess-noise contribution to the shot noise limits the benefits of high avalanche gain.[21]

The FAR of an APD is often dominated by the excess noise of the dark-current contribution and the background-signal contributions. Furthermore, as introduced above, the distribution of the gain—not just its average value—has an impact on sensitivity.[22] Conventional InGaAs/InP APDs typically have bulk InP multiplication layers characterized by an ionization coefficient ratio of $k \sim 0.4$, which parameterizes the McIntyre excess-noise equation.[21] Voxtel has developed a multistage APD, the single-carrier-multiplication APD, which has gains exceeding 50 with excess noise characterized by $k \sim 0.02$. Figure 3 shows the possibilities of improved sensitivity that can be achieved in such APDs by allowing for lower threshold settings with lower FAR.

5.2.1 *Scanned lidar single-element InGaAs APD photoreceivers*

When the FOV of the lidar photoreceiver is matched to the laser, background noise and susceptibility to multiple scattering factors are reduced, and long-range detection is achieved. Figure 6 shows a picture of one of Voxtel's ROX™ InGaAs APD-based lidar photoreceivers, which integrates an InGaAs APD detector, an amplification and pulse-processing application-specific integrated circuit, and temperature-compensating biasing circuits, within the hermetic TO-8 package.[23] In these photoreceivers, the TIA bandwidth is much smaller

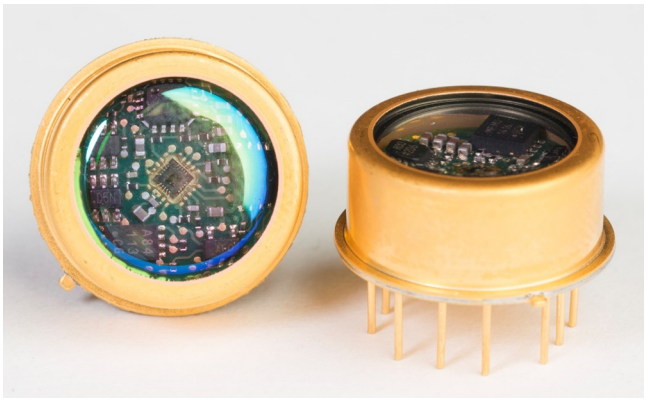

Fig. 6 Our Voxtel ROX APD laser-ranging photoreceiver includes in package temperature compensation and calibration.

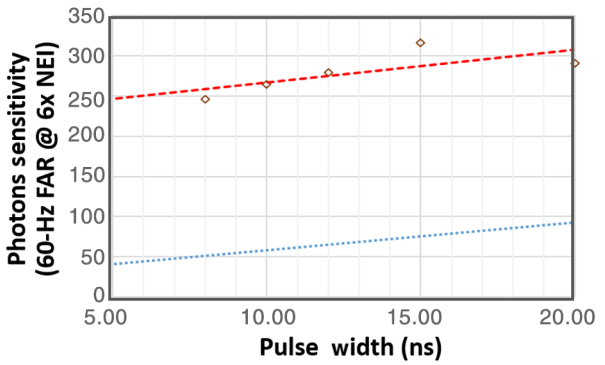

Fig. 7 Measured sensitivity of an InGaAs APD photoreceiver shown as a function of pulse width. Here the higher conversion efficiency of the readout IC (ROIC) increases sensitivity for shorter pulse returns. The threshold sensitivity for 60-Hz FAR (red line; top) is ~6× the NEI (shown for reference; blue line; bottom).

than that of the photodiode (typically, a few gigahertz), and it defines the noise bandwidth. Examples of the sensitivity calculations for a Voxtel single-element InGaAs 250-μm collection area APD detector as a function of pulse width are shown in Fig. 7; the noise-equivalent input (NEI) is ~25 photons, about eight times lower than the 210-photon threshold sensitivity (30 Hz FAR).

5.2.2 *Staring lidar and step-stare lidar two-dimensional InGaAs photoreceiver focal plane array*

APDs of this type can also be made in arrays. Figure 8 shows a picture of Voxtel's VX-806 lidar 128 × 128-element FPA, which captures the time and amplitude of three pulse returns in each pixel. The input-referred noise of 36 e^- is made possible by the high conversion gain of the in-pixel amplifiers and the low capacitance of the linear-mode-APD InGaAs detector elements. With an 80% quantum efficiency, the APDs, when operated at a gain of $M = 20$, allow for an NEI level of below 3 photons $[36/(80\% \times 20) = 2.25$ photons] to be possible. The plot of per-pixel NEI and sensitivity (for 30 Hz and 10 kHz FAR across the entire array) is shown in Fig. 9, as a function of gain. As can be seen, due to the increased excess-shot noise of the dark current, there is an upper limit to useful APD gain. At higher operating gain, the positive skew of the pulse distribution of the avalanche

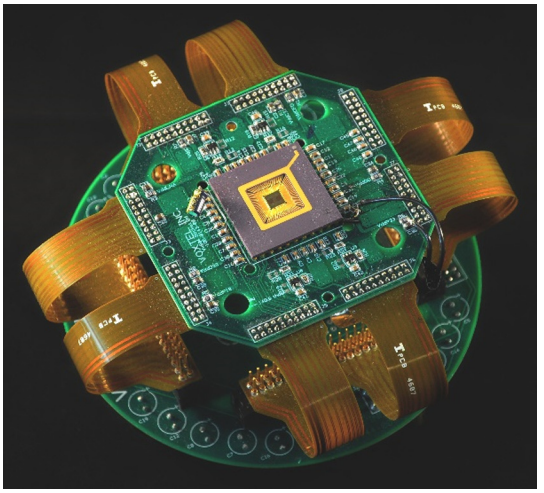

Fig. 8 InGaAs lidar FPA with 128 × 128 elements capable of capturing three timestamps with 200-ps time resolution.

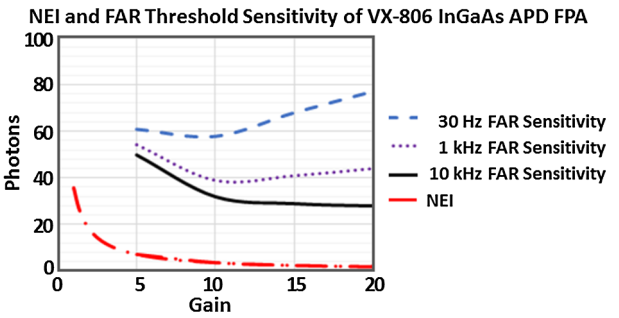

Fig. 9 NEI as a function of gain for various laser-pulse widths for Voxtel's VX-806 InGaAs APD ROIC.

gain process leads to an increase in excess noise. These effects can be mitigated by using a lower threshold setting and using multipulse processing to enhance receiver sensitivity.

5.3 *Mechanical and Nonmechanical Scanners*

Rotating-mirror systems are high performance and, to date, have provided the primary test bed and development platform for the use of lidar in autonomous vehicles.[3] To transition from systems like these to low-cost, compact lidar systems that can fit within the body panels of vehicles, developers are considering a number of alternatives.

Traditional laser beam-steering systems (or scanners) are bulky, power-hungry, and vibration-prone mechanical systems, and new devices—with ultralow size, weight, and power—for electro-optic laser beam steering are needed. The ability to incorporate high mechanical stability and minimal hardware to steer a laser beam from its source to its target quickly, efficiently, and precisely will allow laser scanning—both in transmit and receive modes—to be used almost anywhere.

Alternative solutions to mechanical beam steering that have been explored include microlens arrays, microelectromechanical systems,[24,25] liquid-crystal polarization gratings,[26] holographic glasses, and birefringent prisms. All of these approaches suffer from one or more of the following limitations: low throughput, scattering, small steering angle/aperture, high fabrication cost, and large size/weight.

Fig. 10 Voxtel's laser-ranging sensor integrates a DPSS laser and highly sensitive SWIR photoreceivers.

5.4 *Calibration and Clutter Rejection*

To enable processors to perform the split-second decision making required for assisted-driver and self-driving cars, the sensor package must provide accurate 3-D data. This requires compensation for optical distortions, scanner pointing errors, mounting alignment, detector nonunformity, nonlinearity due to signal amplitude as a function of range, target reflectance, and angle, as well as georeferencing errors.

6 Conclusion

In this work, key lidar sensor parameters, including operating wavelength, pulse energy, pulse frequency, receiver format, and receiver sensitivity, were optimized for the design of a 360-deg eyesafe lidar system capable of 220-m range. Due to the higher MPE, along with less scattering and reduced solar clutter, the 1.5-μm spectral range allows commercially available InGaAs APD detector technologies and erbium-doped DPSS lasers to be used in compact cost-effective sensor configurations (e.g., see Fig. 10). Due to the efficiencies gained by using higher-pulse-energy eyesafe lasers, the cost of this lidar technology scales more readily than lidar technologies that employ 905-nm emitters and detectors. A variety of scanning solutions are currently being evaluated to provide biaxial or coaxial sensor configurations.

References

1. Frost & Sullivan, "LiDAR: driving the future of autonomous navigation —analysis of LiDAR technology for advanced safety," p. 31, Frost & Sullivan (9 February 2016).
2. Frost & Sullivan, "LIDAR-based strategies for active safety and automated driving from major OEMs in Europe and North America," p. 60, Frost & Sullivan (August 2015).
3. Velodyne LiDAR, "Velodyne LiDAR HDL-64E high definition real-time 3D LiDAR," Velodyne LiDAR, Inc., Morgan Hill, California, http://velodynelidar.com/docs/datasheet/63-9194%20Rev-E_HDL-64E_S3_Spec%20Sheet_Web.pdf (2016).
4. S. Higgins, "Quanergy's solid-state LiDAR: details from CES," SPAR 3D, 2016, http://www.spar3d.com/news/hardware/vol14no2-quanergy-solid-state-lidar-details/.
5. Velodyne LiDAR, "Puck real-time 3D LiDAR sensor," Velodyne LiDAR, Inc., Morgan Hill, California, http://velodynelidar.com/docs/datasheet/63-9229_Rev-E_Puck%20_Spec%20Sheet_Web.pdf (2017).
6. G. Michael, V. Venugopalan, and K. Reddy, "Multi-modal sensor registration for vehicle perception via deep neural networks," *High Performance Extreme Computing Conference (HPEC)*, IEEE (2015).
7. P. Latorre-Carmona et al., "Three-dimensional imaging with multiple degrees of freedom using data fusion," *Proc. IEEE* **103**(9), 1654–1671 (2015).
8. International Electrotechnical Commission, "International standard IEC 60825: safety of laser products," Edition 1.2, IEC, Geneva, Switzerland, https://shop.textalk.se/shop/ws26/40626/files/full_size_-_for_start_page_banner/iec60825-1%7Bed1.2%7Den.pdf (2001).
9. J. D. Spinhirne, "Micro pulse lidar," *IEEE Trans. Geosci. Remote Sens.* **31**(1), 48–55 (1993).
10. J. A. Reagan, "New generation lidars to support aerosol radiation/climate forcing studies," *Proc. IEEE Int. Geosci. Remote Sens. Symp.* **3**, 2313–2315 (1995).
11. M. U. Piracha et al., "Range resolved lidar for long distance ranging with sub-millimeter resolution," *Opt. Express* **18**(7), 7184–7189 (2010).
12. N. J. Krichel, McCarthy A., and G. S. Buller, "Resolving range ambiguity in a photon counting depth imager operating at kilometer distances," *Opt. express* **18**(9), 9192–9206 (2010).
13. P. F. McManamon, "Review of ladar: a historic, yet emerging, sensor technology with rich phenomenology," *Opt. Eng.* **51**(6), 060901 (2012).
14. S. O. Rice, "Mathematical analysis of random noise," *Bell Syst. Tech. J.* **23**(3), 282–332 (1944).
15. S. O. Rice, "Mathematical analysis of random noise," *Bell Syst. Tech. J.* **24**(1), 46–156 (1945).
16. R. J. McIntyre, "Multiplication noise in uniform avalanche diodes," *IEEE Trans. Electron. Dev.* **13**(1), 164–168 (1966).
17. G. M. Williams et al., "Time resolved gain and excess noise properties of InGaAs/InAlAs avalanche photodiodes with cascaded discrete gain layer multiplication regions," *J. Appl. Phys.* **113**(9), 093705 (2013).
18. R. J. McIntyre, "The distribution of gains in uniformly multiplying avalanche photodiodes: theory," *IEEE Trans. Electron. Dev.* **19**(6), 703–713 (1972).
19. G. M. Williams, Jr., "Limitations of Geiger-mode arrays for Flash LADAR applications," *Proc. SPIE* **7684**, 768414 (2010).
20. P. F. McManamon et al., "A comparison flash lidar detector options," *Proc. SPIE* **9832**, 983202 (2016).
21. R. J. McIntyre, "A new look at impact ionization-part I: a theory of gain, noise, breakdown probability, and frequency response," *IEEE Trans. Electron. Dev.* **46**(8), 1623–1631 (1999).
22. G. M. Williams et al., "Increased gain InGaAs avalanche photodiode with reduced excess noise achieved through asymmetric carrier modulation," *J. Appl. Phys.* (2013).
23. Voxtel, Inc., "ROX™ Rx series—lowest cost, best performance LRF receivers," Voxtel, Inc., Beaverton, Oregon, http://voxtel-inc.com/files/LRF-Receiver-RVC1-JIAC-100-MHz-75-um.pdf (2015).
24. T. Sandner et al., "Hybrid assembled micro scanner array with large aperture and their system integration for a 3D ToF laser camera," *Proc. SPIE* **9375**, 937505 (2015).
25. M. Helmer et al., "Challenges for MEMS based scanning laser system," in *11th Int. Symp. on Automotive Lighting–ISAL 2015–Proc. of the Conf.*, Vol. 16, Herbert Utz Verlag (2015).
26. S. R. Davis et al., "A lightweight, rugged, solid state laser radar system enabled by non-mechanical electro-optic beam steerers," *Proc. SPIE* **9832**, 98320K (2016).

George M. Williams, Jr., is the president of Voxtel, Inc. in Beaverton, Oregon, USA. Over the last 30 years, he has been involved in researching, designing, and manufacturing advanced infrared focal plane arrays, image-intensified night-vision systems, low-light-level silicon imagers, avalanche photodiode detectors and photoreceivers, and ladar sensors. He previously has worked at PixelVision, Inc., SITe, Inc., Tektronix, ITT Night Vision, Photon Research Associates, and New England Research Center.